Bioactive Materials 17 (2022) 394–405

Contents lists available at ScienceDirect

Bioactive Materials

journal homepage: www.keaipublishing.com/en/journals/bioactive-materials

Black Mn-containing layered double hydroxide coated magnesium alloy for osteosarcoma therapy, bacteria killing, and bone regeneration

Dongdong Zhang [a,b,1], Shi Cheng [c,1], Ji Tan [a], Juning Xie [c], Yu Zhang [c,**], Shuhan Chen [a,b], Huihui Du [a,b], Shi Qian [a,b,e], Yuqing Qiao [a], Feng Peng [c,***], Xuanyong Liu [a,b,d,e,*]

[a] State Key Laboratory of High Performance Ceramics and Superfine Microstructure, Shanghai Institute of Ceramics, Chinese Academy of Sciences, Shanghai, 200050, China
[b] Center of Materials Science and Optoelectronics Engineering, University of Chinese Academy of Sciences, Beijing, 100049, China
[c] Medical Research Center, Department of Orthopedics, Guangdong Provincial People's Hospital, Guangdong Academy of Medical Sciences, Guangzhou, Guangdong, 510080, China
[d] School of Chemistry and Materials Science, Hangzhou Institute for Advanced Study, University of Chinese Academy of Sciences, 1 Sub-lane Xiangshan, Hangzhou, 310024, China
[e] Cixi Center of Biomaterials Surface Engineering, Ningbo, 315300, China

ARTICLE INFO

Keywords:
Biodegradable magnesium
Layered double hydroxides
Anti-tumor
Anti-bacterial
Bone regeneration

ABSTRACT

Osteosarcoma (OS) tissue resection with distinctive bactericidal activity, followed by regeneration of bone defects, is a highly demanded clinical treatment. Biodegradable Mg-based implants with desirable osteopromotive and superior mechanical properties to polymers and ceramics are promising new platforms for treating bone-related diseases. Integration of biodegradation control, osteosarcoma destruction, anti-bacteria, and bone defect regeneration abilities on Mg-based implants by applying biosafe and facile strategy is a promising and challenging topic. Here, a black Mn-containing layered double hydroxide (LDH) nanosheet-modified Mg-based implants was developed. Benefiting from the distinctive capabilities of the constructed black LDH film, including near-infrared optical absorption and reactive oxygen species (ROS) generation in a tumor-specific microenvironment, the tumor cells and tissue could be effectively eliminated. Concomitant bacteria could be killed by localized hyperthermia. Furthermore, the enhanced corrosion resistance and synergistic biofunctions of Mn and Mg ions of the constructed black LDH-modified Mg implants significantly facilitated cell adhesion, spreading and proliferation and osteogenic differentiation *in vitro*, and accelerated bone regeneration *in vivo*. This work offers a new platform and feasible strategy for OS therapeutics and bone defect regeneration, which broadens the biomedical application of Mg-based alloys.

1. Introduction

Osteosarcoma (OS) is a primary malignant neoplasm of the skeleton that usually arises from the metaphyses of the long extremity bone and often occurs in adolescents [1,2]. The impact of OS is devastating, often leading to a severe decline in patients' quality of life and survival rates [3,4]. In clinics, the traditional treatment of OS is surgical resection, followed by chemo/radiotherapy to kill residual tumor cells [5]. However, these problems include chemo/radiation resistance, severe side effects, and large bone defects that cause endless new suffering to patients [6]. Therefore, considering the clinical requirements of tumor tissue resection and simultaneous regeneration of bone defects, it is an urgent need to develop new treatment platforms for desirable therapeutic effects.

The development of orthopedic biomaterials with well-defined functions may regulate biochemical processes and have become a

Peer review under responsibility of KeAi Communications Co., Ltd.
* Corresponding author. State Key Laboratory of High Performance Ceramics and Superfine Microstructure, Shanghai Institute of Ceramics, Chinese Academy of Sciences, Shanghai, 200050, China.
** Corresponding author.
*** Corresponding author.
E-mail addresses: zhangyu@gdph.org.cn (Y. Zhang), pengfeng@gdph.org.cn (F. Peng), xyliu@mail.sic.ac.cn (X. Liu).
[1] These authors contributed equally to this work.

https://doi.org/10.1016/j.bioactmat.2022.01.032
Received 5 November 2021; Received in revised form 17 January 2022; Accepted 18 January 2022
Available online 27 January 2022

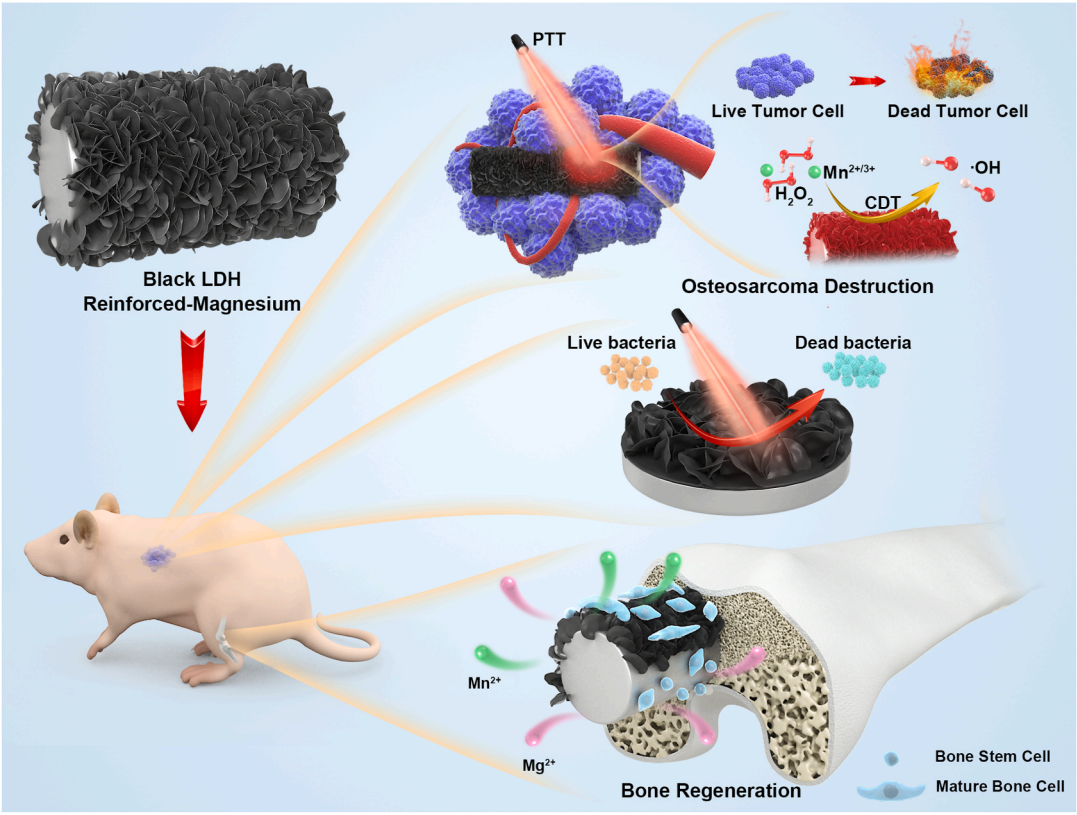

Scheme 1. Stepwise therapeutic strategy for osteosarcoma destruction, antibacteria, and followed bone regeneration.

novel and effective treatment strategy [7–10]. Magnesium (Mg)-based materials with excellent osteopromotive properties, unique biodegradability, and suitable biomechanical properties are candidates for the next generation of metal implants [10–14]; they are notably superior to polymer and ceramic implants in terms of their physical and mechanical properties [15–17]. However, studies on the designs and applications of Mg-based implants for local bone tumor therapy, in contrast, are still in their infancy [18,19]. In addition, the low standard electrode potential/corrosion potential of Mg-based materials restricts their application as an orthopedic biomaterial [20–22]. They can easily cause alkalinity and overproduction of hydrogen gas and Mg ions near the embedded surroundings, and these factors result in poor biocompatibility and premature loss of mechanical properties [23–25]. Furthermore, bacterial infection is another obstacle that limits their widespread applications [26]. Loading drugs or ions, is currently the most widely used strategy to address this issue [27]. However, uncontrolled release of these substances could cause systemic toxicity and side-effects, especially with the rapid corrosion of Mg substrates [28]. Therefore, to fulfill the clinical application of OS therapy, several requirements should be met: (i) the anti-corrosion performance and biocompatibility of Mg-based implants should be improved as a primary concern, (ii) selective antitumor and osteogenic functions should be endowed, and (iii) antibacterial ability should be considered by using a safe strategy. Considering the potential of infection during therapy and repair processes, the prospective therapy needs to be antibacterial. However, to our best knowledge, this kind of biodegradable metal material with such multifunctionality has not yet been reported.

The rapid development of nanotechnology opens new areas for functionalization of implants and extends their applications [29–32]. Layered double hydroxides (LDHs) nanosheets are two-dimensional (2D) materials with high tunability (size, metal cations, and interlayer anions) and excellent ion-exchange capability [33]. Owing to these unique properties, LDHs are easy to design and functionalize. Excellent properties, including photothermal conversion, Fenton catalysis, photocatalysis, and electrocatalysis, have been developed for LDH-based materials [34,35]. In addition, they have garnered extensive attention for biomedical applications, such as cancer therapy, bioimaging, antibacterial, osteogenesis, and biodegradation control [36,37]. Therefore, LDHs may be promising coating materials for the surface biofunction of Mg-based implants. Among the various types of LDHs, Mn-based LDHs have received particular attention because of their valence-dependent physicochemical properties (photothermal and catalytic properties) and biofunctions (antibacterial and osteopromotive properties) of Mn-containing materials [38–41]. In addition, according to the dual criteria of "biodegradability" and "biocompatibility" proposed by Zheng et al., to screen for elements with potential applications as biodegradable metals, Mn can be used in quantities greater than 1 mg in humans and is, therefore, safe and potentially beneficial to human health [16].

Comprehensively considering the integration of biodegradation control, OS destruction, antibacterial characteristics, and bone defect regeneration using a bio-safety method to meet the high demand of clinical requirements, we developed a black Mn-containing LDH film-modified biodegradable Mg alloy for sophisticated OS therapeutics and bone defect regeneration (Scheme 1). First, the corrosion resistance, biocompatibility, photothermal properties, and chemodynamic effect of the black LDH with various Mn contents were investigated. Subsequently, the photothermal/chemodynamic-therapeutic capabilities for tumor cells and tissues of the black LDH-modified Mg alloy were studied *in vitro* and *in vivo*. In addition, their photothermal antibacterial properties were studied *in vitro*. Furthermore, the osteopromotive properties of the black LDH film were assessed *in vitro* and *in vivo*.

Table 1
Element composition of AZ31 used in this work.

Mg (wt.%)	Al (wt.%)	Zn (wt.%)	Mn (wt.%)	Ca (wt.%)	Si (wt.%)	Fe (wt.%)	Cu (wt.%)	Ni (wt.%)
96.02429	2.77	0.93	0.27	0.00001	0.0017	0.0018	0.0016	0.0006

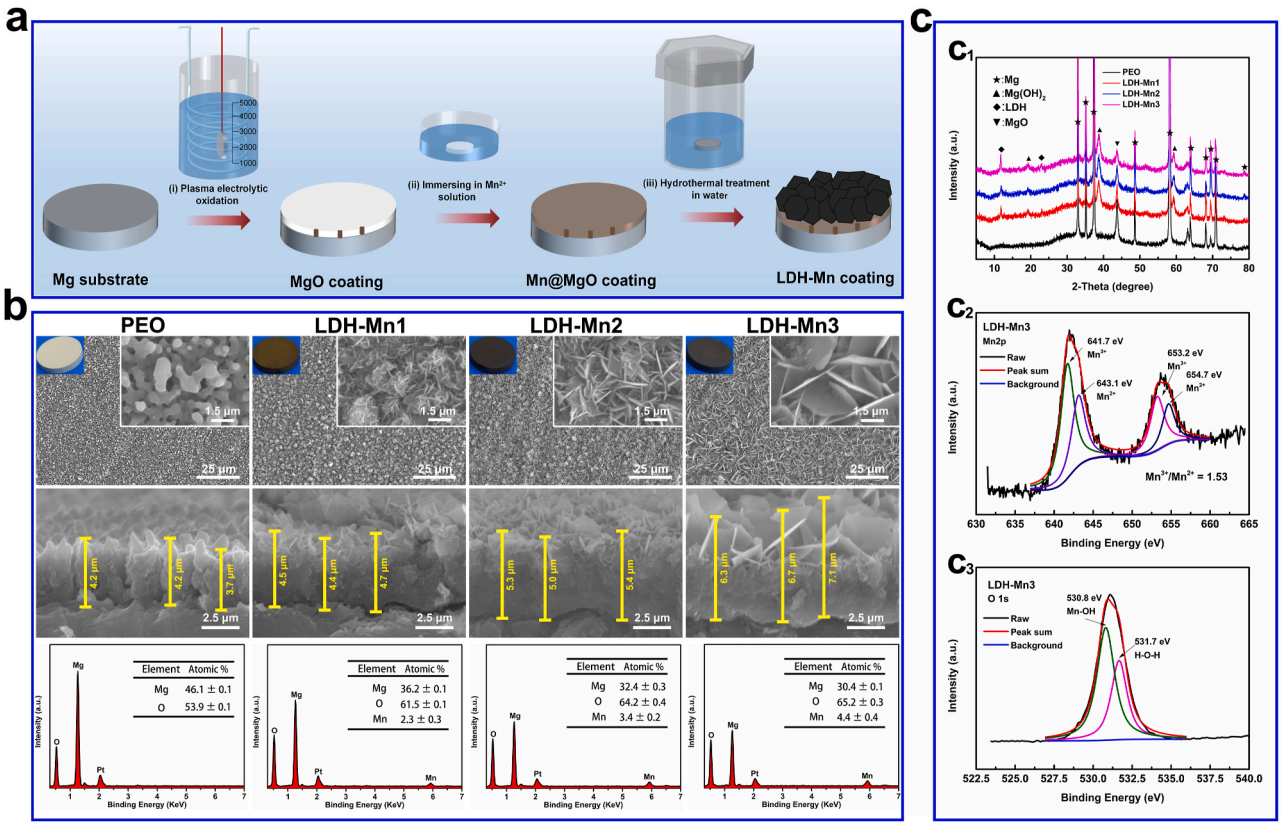

Fig. 1. Schematic illustration of **s**ynthesis process for the Mg-Mn LDH coatings on magnesium alloy (a). Surface morphologies, cross-sectional SEM images and EDS spectra of the various samples (b). XRD patterns of the various samples (c_1). High-resolution XPS spectra for Mn 2p (c_2) and O 1s (c_3) of the LDH-Mn3 sample.

2. Materials and methods

2.1. Materials

AZ31 sheets (10 mm in diameter, 2 mm in thickness) were adopted as the raw substrates *in vitro*. AZ31 rods (1 mm in diameter, 4 mm and 10 mm in length) were used as the substrates in tumor destruction and bone formation tests *in vivo,* respectively. The element composition of AZ31 used in this work is displayed in Table 1. Sodium glycerophosphate ($C_3H_7Na_2O_6P$), Potassium hydroxide (KOH), and Manganese chloride ($MnCl_2.4H_2O$) was used to prepare the coatings.

2.2. Sample preparation

Plasma electrolytic oxidation (PEO)/LDH coatings were prepared via a novel method combining PEO process, immersion treatment, and hydrothermal treatment, as shown in Fig. 2a. In preparation of PEO sample, the electrolyte consists of 10 g/L $C_3H_7Na_2O_6P$ and 12.5 g/L KOH. The processes were performed at a constant current of 0.8 A, frequency of 1000 Hz and duty cycle of 10%. The reaction was stopped at a voltage of 340 V. Next, immersing the PEO samples in 12 g/L of $MnCl_2.4H_2O$ aqueous solution for 3, 6, and 9 h. Last, placing the processed samples in water for 8 h at 120 °C. The as-prepared samples were denoted as LDH-Mn1, LDH-Mn2, and LDH-Mn3, respectively.

2.3. Characterizations

Surface topographies were characterized by the scanning electron microscopy (SEM; S-3400 N, HITACHI, Japan). Chemical compositions were investigated using energy dispersive spectrometry (EDS; IXRF-550i, IXRF SYSTEMS, USA). Crystalline phase was measured by X-ray diffraction (XRD; D2PHASE, BRUKER, USA). X-ray photoelectron spectroscopy (XPS; RBD upgraded PHI-5000C ESCA system, USA) was used to characterization of the surface chemical states of LDH-Mn3 sample.

2.4. Corrosion tests

Tafel polarization curves were tested using an electrochemical workstation (CH1760C) at a scan rate of 10 mV s^{-1} from −2 V to 0 V. In hydrogen evolution test, different groups with four parallel samples were immersed in 300 mL 0.9 wt % NaCl at 37 °C, and the released hydrogen was measured. The samples were immersed in 4 mL PBS solution at 37 °C, the extract was collected, and then fresh phosphate buffer solution (PBS) was added daily. The pH of all the extracts were measured using a pH meter. The corroded morphologies of the samples were obtained by immersing the samples in 2 mL of 0.9 wt % NaCl solution at 37 °C for 7 days, and then the immersed samples were cleaned three times with ethanol and observed by SEM.

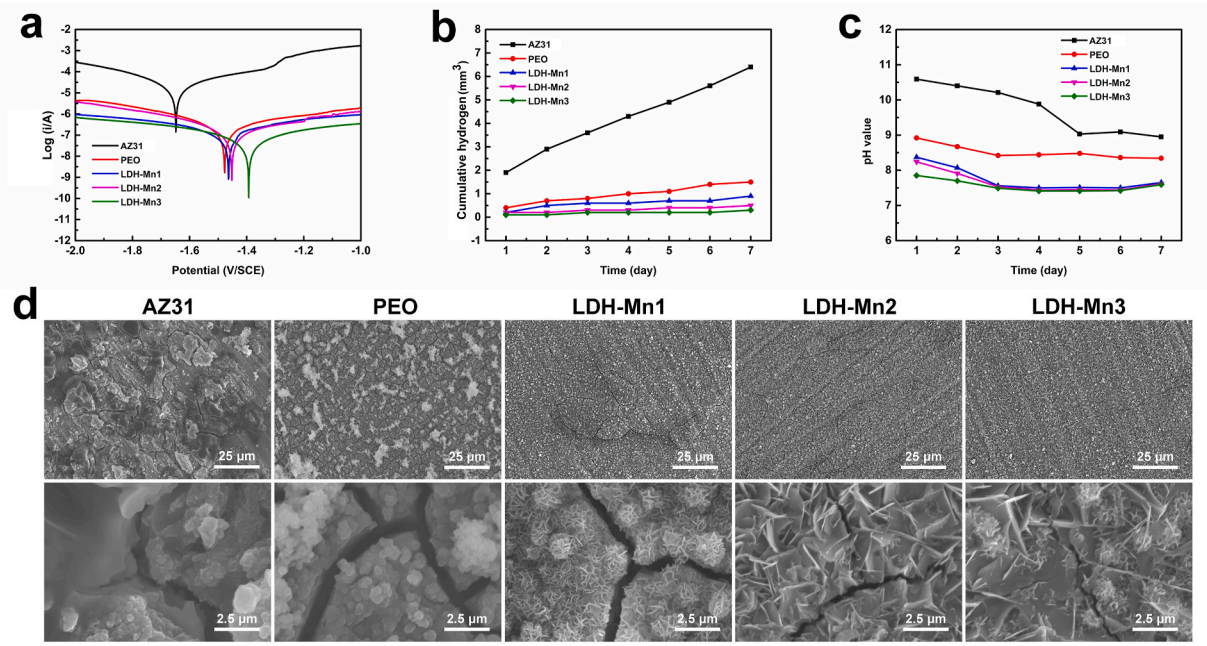

Fig. 2. Corrosion resistance studies: (a) potentiodynamic polarization curves; (b) hydrogen release test; (c) pH value evolution; and (d) corrosion morphologies of the various samples.

2.5. Photothermal effect

The samples were placed in 24-well plates with 500 μL PBS, and the temperature variation under irradiation at 808 nm near infrared (NIR) light (0.8 W/cm^2) was monitored using a FLIR ONE infrared thermal instrument.

2.6. Oxidase-like activity assessment

The oxidase-like activities of the various samples were studied by evaluating the catalytic performance of 3,3′,5,5′-tetramethylbenzidine (TMB) in 0.9 wt % NaCl solution. In brief, the samples were placed in a 24-well plate with 4 mM TMB and 100 μM H_2O_2 at room temperature for incubating 30 min. Subsequently, 100 μL of the solution mentioned above was transformed to a 96-well plate and the absorbance was measured by Cytation 5 Multi-Mode Reader (BioTek, USA).

2.7. Cytocompatibility

The cytocompatibility test were performed according to previous study [15]. Briefly, MC3T3-E1 cells were used to evaluate the initial cell adhesion, proliferation, and viability. Cells (2.0×10^4 cells/mL) were seeded onto the sterilized samples and cultured for 1, 4, and 24 h. Then, the cells were fixed with 4% paraformaldehyde (PFA) solution for 10 min, followed by staining with fluorescein isothiocyanate (FITC)--phalloidin and 4′,6-diamidino-2-phenylindole (DAPI) for F-actin and the nuclei indicating, respectively. Finally, the cells were examined using confocal laser scanning microscopy. Cells (5.0×10^4 cells/mL) were seeded onto the samples for 1, 4, and 7 days to measured cell proliferation rates using the AlamarBlue™ assay. Cells (2.0×10^4 cells/mL) were cultured on the samples for 4 days to evaluate live/dead staining. Briefly, 100 μL PBS mixed with calcein-AM (2 μM) and propidium iodide (PI, 5 μM) was added to each sample and after staining the cells for 15 min, they were examined using fluorescence microscopy.

2.8. Protein adsorption

The samples were cleaned twice with ultrapure water and placed in a 24-well plate. Then, 1 mg/mL bovine serum albumin (BSA) solution was added and incubated for 24 h at 37 °C. Afterward, the samples were rinsed with PBS solution, and the adsorbed BSA was eluted with 2 wt % lauryl sodium sulfate. Subsequently, 100 μL of the mixture solution was transformed to a 96-well plate and its absorbance at 560 nm was measured.

2.9. Hemolysis assay

The hemolysis test were performed according to previous study [15]. Briefly, the samples were placed in a 24-well plate with 1.5 mL saline solution for 30 min at 37 °C. Then, 30 μL diluted blood (fresh human blood/aline solution = 4/5) was added and the mixture was incubated for 60 min. Furthermore, 30 μL diluted blood was added to saline and distilled water as the negative and positive controls, respectively. Then, the mixtures were collected, centrifuged at 3000 rpm for 5 min, and the absorbance of the supernatant at 545 nm was detected. The hemolysis rate was calculated using the equation: hemolysis rate = $(A_{sample}\text{-}A_{negative})/(A_{positive}\text{-}A_{negative}) \times 100\%$.

2.10. Antibacterial properties

The antibacterial test were performed according to previous study [15]. Briefly, 500 μL of a diluted bacterial suspension (*S. aureus* and *E. coli*, 10^7 CFU/mL) was co-incubated with the samples for 12 h. Subsequently, the samples were irradiated to NIR irradiation (0.8 W/cm^2, 10 min), in NIR (+) group. Then, the samples were transferred to tubes with 4 mL saline solution and dissociated adhered bacteria. Next, the solutions were diluted 100-fold and 100 μL volume of the diluted bacterial samples was spread onto a standard agar culture plate, which was incubated at 37 °C for 18 h. The bacteria that adhered to the samples were fixed with 2.5 v% glutaraldehyde for 4 h, and then dehydrated in ethanol and the bacterial morphology was observed using SEM.

2.11. In vitro tumor killing

Sao-2 tumor cells (5.0×10^4 cells/mL) were seeded on the surface of samples in a 24-well plate for 4 days. Then, the wells were exposed to NIR irradiation in NIR (+) (0.8 W/cm^2, 10 min) groups. Afterward, the cells activity was measured by AlamarBlue™ assay and Live/Dead

staining.

2.12. In vivo tumor destruction

All animal studies were performed in accordance with the Guidelines for Care and Use of Laboratory Animals of Guangdong Provincial People's Hospital and approved by the Institutional Animal Care and Use Committee of Guangdong Provincial People's Hospital (KY2020-018-01-01). Balb/c nude mice (male, 4-6 weeks) were used to construct tumor model. UMR106 tumor cells (2×10^6 cells) were injected into the back of the mice. When the tumors grew up to a volume of 250 mm^3, the mice were assigned to three groups: AZ31; LDH-Mn3; and LDH-Mn3 + NIR. AZ31 and LDH-Mn3 specimen were inserted into the tumor center. LDH-Mn3 + NIR group were irradiated with NIR (1.0 W/cm^2, 5 min) every day after the surgery. The surface temperature of irradiated groups was monitored using an infrared thermal instrument. The tumor length and width were measured every day and were used to calculate tumor volume Tumor volume (TV) = (length × $width^2$)/2. The relative tumor volume (Vr) was equal to V/V0 (V0 = tumor volume before the first time of irradiation). The tumors were separated from the back of mice after 7 days treatment, and then photographed. Then the obtained tissue were fixed in formalin, embedded in paraffin and sliced. The sliced tissues were subjected to hematoxylin and eosin (H&E) staining, deoxynucleotidyl transferase-mediated dUTP nick-end labeling (TUNEL) immunofluorescent staining, and Ki67 immunohistochemical staining.

2.13. Cytocompatibility of extracts

Each specimen was immersed in α-MEM (1 mL) for 24 h at an incubator. Then the culture mediums were collected and used as extracts. C3H10T1/2 cells (2×10^3 cells/well) were cultured in 96-well plates. 6 h later, the culture mediums were removed and the wells were added with various extracts. At days 1, 4, and 7, cell viability was detected using Cell Counting Kit-8 (Dojindo Molecular Technology, Japan) assay.

2.14. Alkaline phosphatase (ALP) activity

C3H10T1/2 cells were cultured on 24-well plates with a concentration of 2×10^4 cells/well. After adhesion for 6 h, the culture medium was replaced with various extracts. 3 and 7 days later, the expression of ALP was evaluated using BCIP/NBT ALP color development kit (Beyotime, China). To quantitatively evaluate ALP activity, the amount of ALP and total protein were measured using ALP Assay Kit (Beyotime Biotechnology, China) and BCA protein quantitation kit (Beyotime, China), respectively. The ALP value was normalized to level of total BCA.

2.15. Extracellular matrix (ECM) mineralization

C3H10T1/2 cells were cultured as mentioned above. At days 7 and 14, Alizarin Red (Cyagen, China) was used to detect the ECM mineralization. Amicroscope system (Olympus, Germany) was used to observe the stained Alizarin Red. The bonded Alizarin Red were then dissolved in sodium phosphate aqueous solution containing cetylpyridinum chloride and the optical density (450 nm) of the solution was measured using a microplate reader (Bio-Tek, USA).

2.16. Quantitative real time-polymerase chain reaction (qRT-PCR)

The total RNA in the cells was extracted using Trizol (SigmaAldrich, USA) and then quantified using nanodrop 2000 (Thermofisher, USA). RNA was then reversely transcribed into cDNA and then mixed with SYBR Green Mastermix and primers. The gene expression was quantified using the 96 Real-Time PCR System (Bio-Rad, USA). The primer sequences of the targeted genes are listed in Table 2.

Table 2
Primer sequences used in quantitative real time-polymerase chain reaction (qRT-PCR).

GENE	Primer Sequence	
	Forward (5'-3')	Reverse (3'-5')
GAPDH	TTCCAGGAGCGAGACCCCACTA	GGGCGGAGATGATGACCCTTTT
ALP	TCCGTGGGCATTGTGACTAC	TGGTGGCATCTCGTTATCCG
COL-I	GCTCCTCTTAGGGGCCACT	ATTGGGGACCCTTAGGCCAT
OCN	GGTAGTGAACAGACTCCGGC	GGCGGTCTTCAAGCCATACT
RUNX2	GACTGTGGTTACCGTCATGGC	ACTTGGTTTTTCATAACAGCGGA
OPN	GACAGTCGAATCCATAGCAGC	AGAGACGACCGCATAAGGAAT

GAPDH, glyceraldehyde 3-phosphate dehydrogenase; ALP, alkaline phosphatase; type I collagen, COL-I; OCN, osteocalcin; RUNX2, RUNX family transcription factor 2.

2.17. Bone implantation

The animal experiments were conducted under the authorization of the Guidelines for Care and Use of Laboratory Animals of South China University of Technology and Animal Ethics Committee of Guangdong Provincial People's Hospital. Eighteen Sprague-Dawley (SD) rats (male, six-week old) were used. For each rat, both of the femurs were implanted with one specimen along the major axis. The femurs were harvested at weeks 4 and 8. Micro-CT (Aloka Latheta LCT-200; HITACHI, Japan) was used to scan the newly formed bone. Bone volume percentage (BV/TV) and trabecular thickness (Tb.Th) were figured using 3D bone morphometric analysis. The femurs were then dehydrated in ethanol and embedded in polymethyl methacrylate (PMMA). The embedded tissues were into slices. After grinded, the slices were stained with Van Geison's solution (VG).

2.18. Statistical analysis

All the *in vitro* and *in vivo* studies were performed at least 4 repeats. Data are presented as the mean ± standard deviation. Differences among groups were analyzed by one-way and two-way ANOVA followed by Tukey's post hoc test using the SPSS 19.0 software. $P < 0.05$ was considered a significant difference.

3. Results and discussion

3.1. Sample synthesis and characterization

In this work, black Mn-containing LDH films were prepared on Mg alloy through a novel two-step method based on our previous study (Fig. 1a) [42]. First, the PEO sample was immersed in an Mn^{2+} solution to fabricate Mn-based hydroxide layers, acting as the Mn-source. In this process, the MgO phase of the PEO coating generated numerous OH^-, surrounding the sample in water when slight corrosion occurred. Then excessive local alkalinity precipitated Mn^{2+} close to the sample surface to form Mn-based hydroxide layers on the PEO coating. Afterward, the Mg-Mn LDH films were grown *in situ* by transforming the Mn-containing layers through hydrothermal treatment in water. The formation mechanism can be described as an ion-substitute hydroxide process: Mg^{2+} released from the MgO phase in the PEO coating are diffused and embedded into the Mn-based hydroxide layer to replace some Mn^{3+}, resulting in excessive positive charges and attracting numerous OH^- to form the charge-balanced LDH.

The surface structures and element compositions of the constructed LDH films were characterized via SEM and EDS, respectively. The raw AZ31 sample showed a flat surface structure (Fig. S1). As shown in Fig. 1b, the PEO coating exhibited a porous structure, and the LDH films presented highly oriented nanosheet structures. With the increase in Mn content from 2.3 ± 0.3% to 4.4 ± 0.4%, the size of LDH nanosheets, as

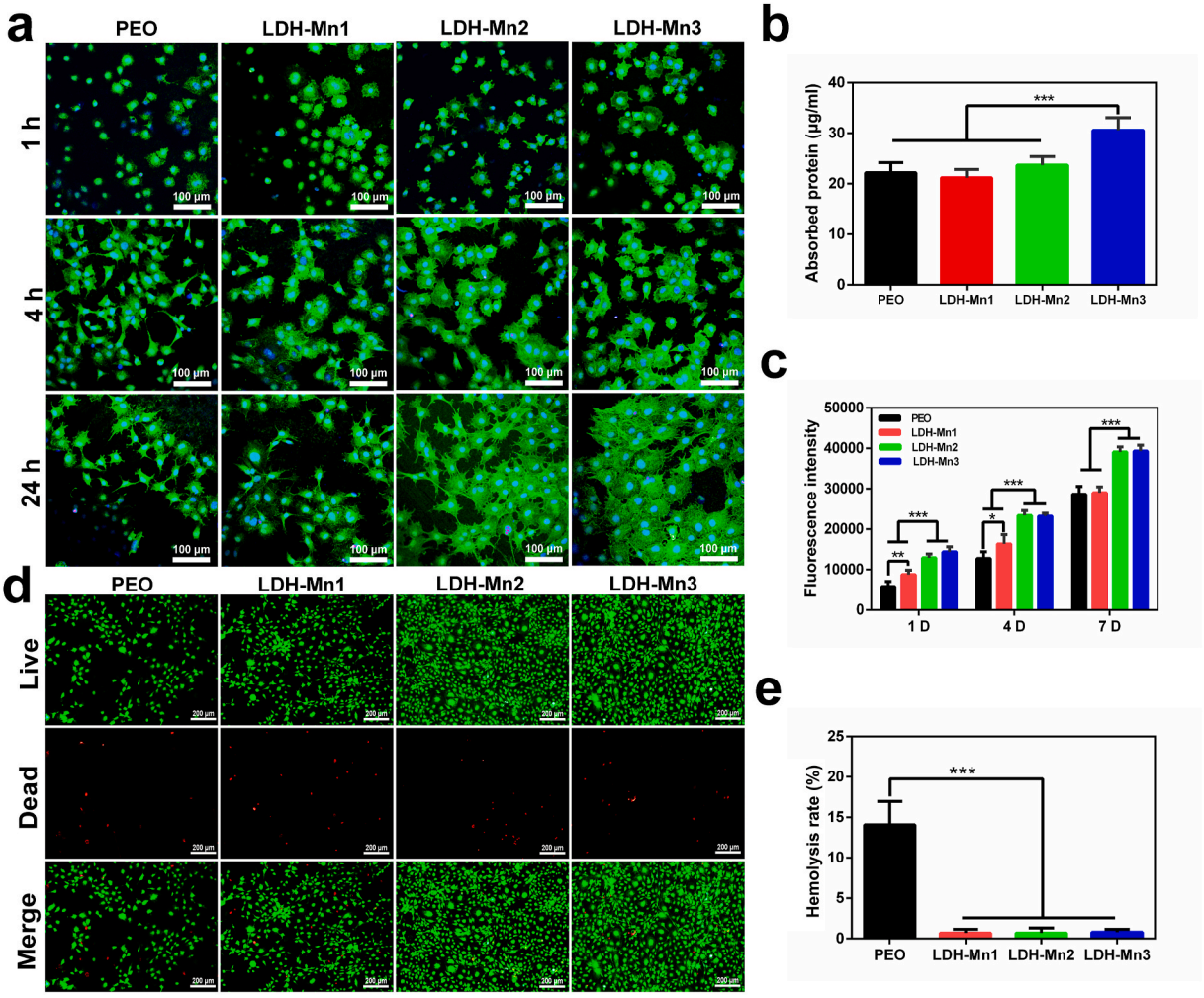

Fig. 3. CLSM images of F-actin stained with FITC (green) and the nucleus stained with DAPI (blue) of MC3T3-E1 cells cultured on the various samples for 1, 4, and 24 h (a). Protein adsorption test of the various samples (b). Fluorescent intensity of AlamarBlue reduced by MC3T3-E1 cells cultured on the various samples for 1, 4, and 7 days (c). Fluoroscopy images of Live/Dead (green/red) staining of MC3T3-E1 cells cultured on the various samples for 4 days (d). Hemolysis rate of the various samples (e).

well as the thickness of the duplex coatings, increased. This change improved the corrosion resistance of the modified Mg alloy specimens. More importantly, the sheets changed from white to black as the content of Mn increased, which demonstrates an excellent photothermal conversion performance.

The phase compositions of the black LDH films were measured using XRD and XPS. The characteristic XRD diffraction peak at approximately 12° signified the (003) crystal face of LDH, reflecting the successful fabrication of the LDH phase on the Mg alloy specimens (Fig. 1c1). The Mn 2p spectrum in the LDH-Mn3 film shows two main peaks, each of which can be divided into two peaks at 641.7/653.2 and 643.1/654.7 eV, belonging to Mn^{3+} and Mn^{2+}, respectively (Fig. 1c2) [43–45]. The O 1s spectrum was divided into two peaks at 530.8 and 531.7 eV, representing Mn–O–H band and surface-adsorbed oxygen, respectively (Fig. 1c3) [43–45]. The above results indicated that the black Mg–Mn (II)–Mn(III) LDH films were formed on the Mg alloy.

3.2. Corrosion resistance

LDH coatings have been developed in recent decades to provide industrial-grade anticorrosion properties to metals, including Mg, Zn, and Al alloys [46]. LDH layers combined with PEO coating are suitable for enhancing the corrosion resistance of Mg [47]. Additionally, LDH nanosheets can completely seal the micropores on the PEO coatings and thus, prevent direct contact of corrosive liquids with the Mg alloy substrate. LDH nanosheet can attract or block Cl^- as an anion container to protect the coating from damage. The corrosion behavior of the LDH samples with AZ31 and PEO coating as the control is presented in Fig. 2. Potentiodynamic polarization curves showed that the corrosion potential of AZ31 shifted positively, while the corrosion current density decreased greatly after surface modification (Fig. 2a). The corrosion resistance of the different samples exhibited the following increasing trend: AZ31 < PEO < LDH-Mn1 < LDH-Mn2 < LDH-Mn3. The hydrogen release and pH value evolution were further measured to investigate the long-term corrosion behavior of each sample (Fig. 2b and c). AZ31 sample exhibited a fast release of hydrogen and a higher pH value, whereas the LDH samples, especially the LDH-Mn3 sample, showed relatively mild corrosion behavior. In addition, the least cracks were observed on LDH-Mn3 sample after immersing in 0.9 wt % NaCl for 7 days, exhibiting best corrosion resistance among all the samples (Fig. 2d). The similar results were also observed on the corrosion morphology of the various samples immersed in dulbecco's modified eagle medium (DMEM) for 14 days (Fig. S2). These results can be attributed to its thicker coating thickness and larger LDH nanosheets.

3.3. In vitro biocompatibility

The cellular activity is closely related to the extracellular

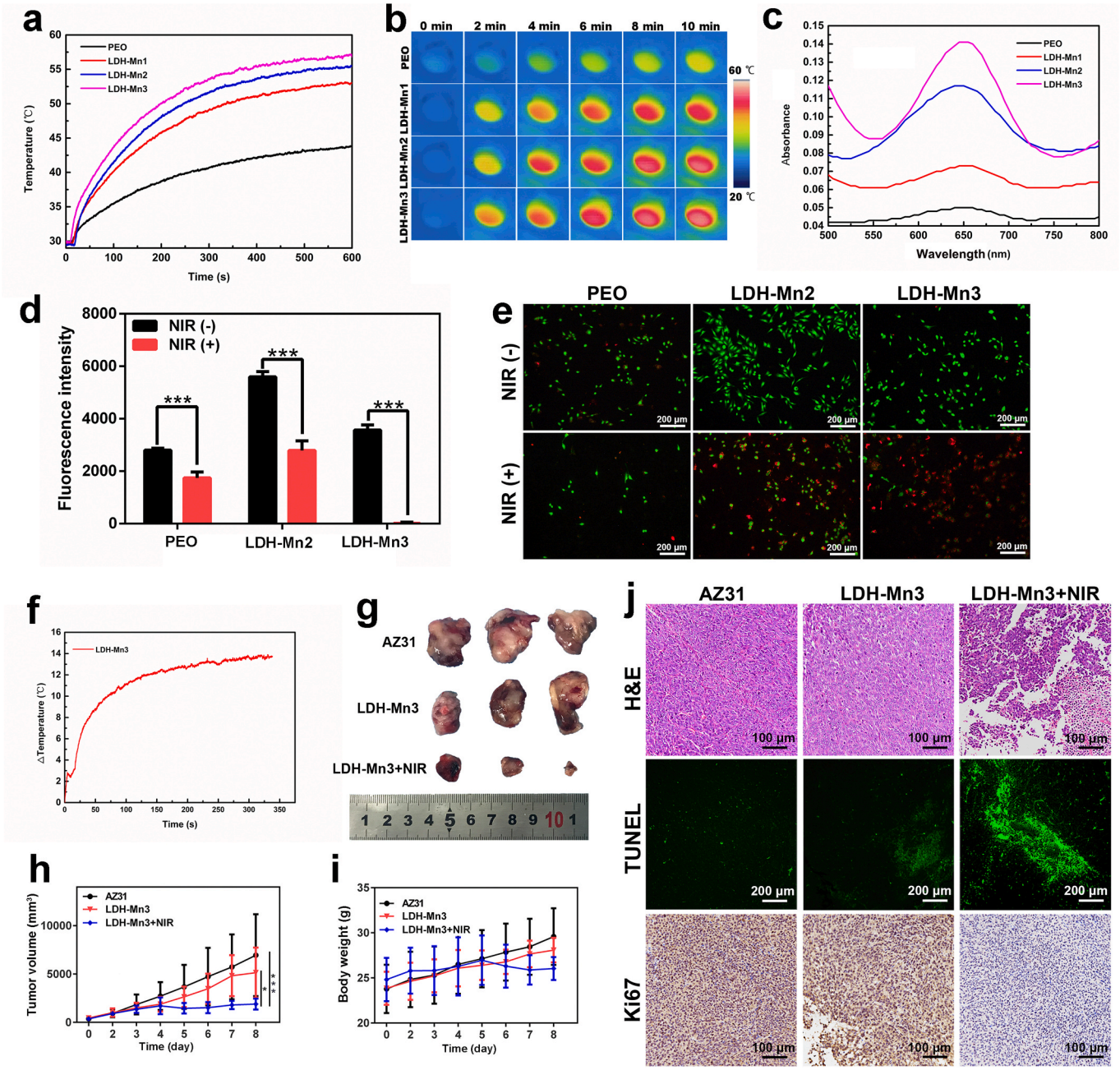

Fig. 4. Temperature elevation curve (a) and corresponding infrared thermographic photographs (b) of the various samples under NIR irradiation (0.8 W/cm^2). Catalytic oxidation of TMB by LDH-Mn1, LDH-Mn2, and LDH-Mn3 with 100 μM H_2O_2 in 0.9 wt % NaCl solution (c). Fluorescent intensity of AlamarBlue reduced by Sao-2 tumor cells cultured on the various samples for 4 days after treated with or without NIR irradiation (d) and the corresponding Live/Dead staining (e). Temperature increase curves of LDH-Mn3 in osteosarcoma tissue under NIR irradiation (1.0 W/cm^2). Photographs of tumor tissue after different treatments in nude mice as described in the figure (g). Time-dependent tumor-growth curves of the mice after different treatments (h). Time-dependent body weight curves of nude mice after different treatments (i). H&E, TUNEL, and Ki67 staining of tumor tissue after different treatments (j).

microenvironment [48]. Hydrogen and excessive Mg^{2+} and OH^- ions are easily produced from the corrosion of bare Mg alloys because of their high chemical activity, considerably inhibiting the surrounding cell activity. Protective coatings can effectively prevent their corrosion to improve the cellular activities, theoretically [49,50]. It should be noted that AZ31 surface has high chemical activity, which makes it difficult for cells to survive. Therefore, PEO sample was used as the control group. Fig. 3a displays the initial cell adhesion behavior. Cells on the PEO and LDH-Mn1 samples showed a spherical shape even after culturing for 24 h. In contrast, cells attached to the LDH-Mn1 and LDH-Mn2 samples exhibited polygon morphology after 4 h of culture and displayed a high degree of spreading after 24 h, especially for LDH-Mn3 samples. As presented in Fig. 3b, LDH-Mn3 sample showed the significant higher protein adsorption capacity than the other samples. Protein adsorption is the first interaction between biomaterials and organisms, further promoting cell adhesion. Besides, AlamarBlue™ assay was performed for the cells attached to various sample surfaces after 1, 4, and 7 days, as displayed in Fig. 3c. The number of cells on the LDH-Mn2 and LDH-Mn3 sheets was significantly higher than that on the other two groups at all three detection time points. A significantly higher number of cells was detected on LDH-Mn1 than PEO sheets on days 1 and 4. On day 7, no significant difference was observed in the cell number between the two groups. Besides, as shown in Fig. 3d, in the live/dead staining test, more alive cells (dyed by green) were observed on the LDH-Mn2 and

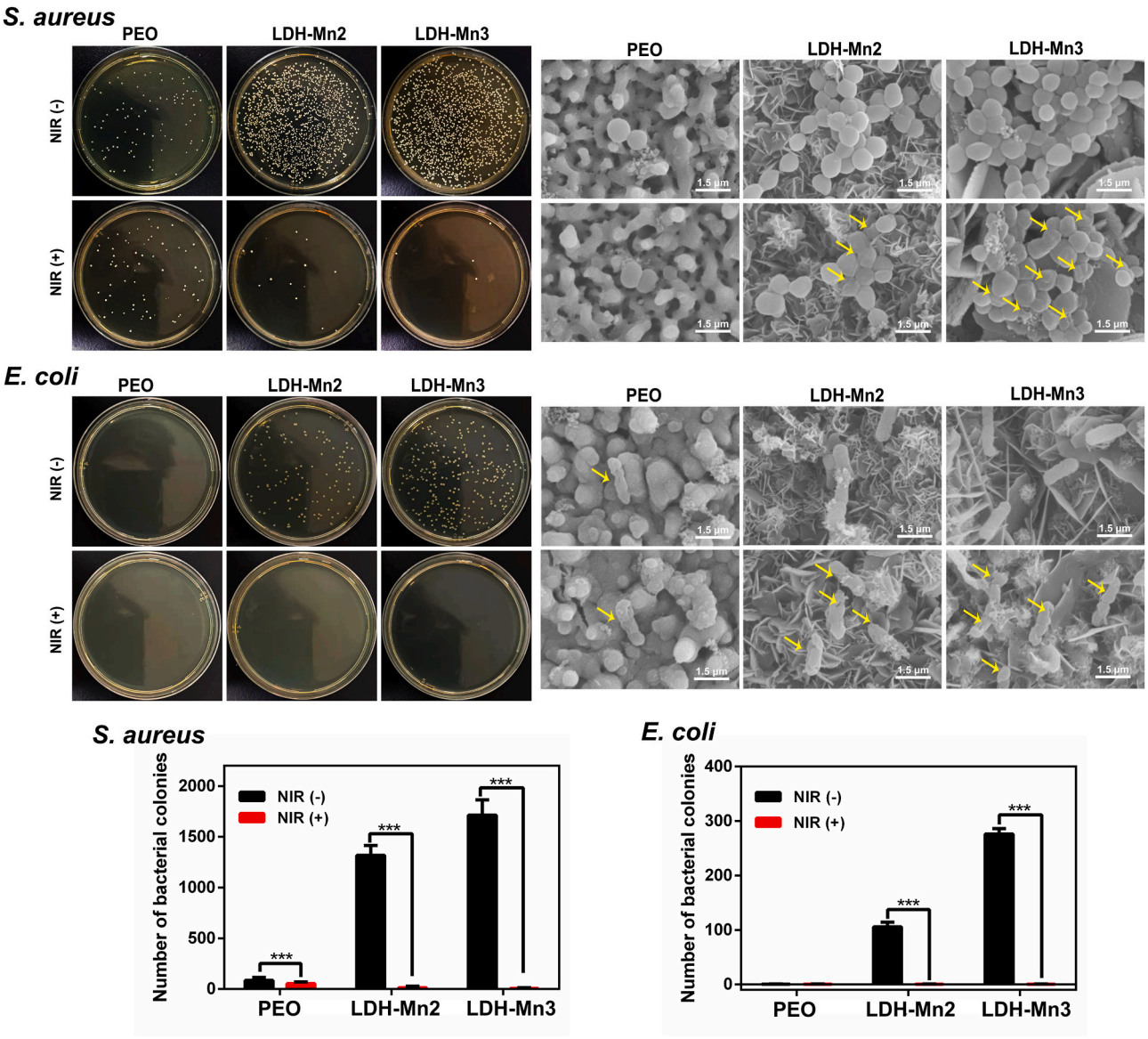

Fig. 5. *In vitro* antibacterial investigation: representative culture images of bacterial colonies and corresponding SEM images of the various samples.

LDH-Mn3 groups due to better anticorrosion performances. The hemolysis rate (HR) value, a critical parameter that is expected to be <5% for clinical applicability, was evaluated. As shown in Fig. 3e, the HR value of the PEO sample was far beyond the acceptable value of 5%, while all LDH-coated samples presented low HR values (below 5%), and no significant difference was observed between them. These results reflected that LDH-Mn2 and LDH-Mn3 samples possess excellent biocompatibility.

3.4. Photothermal and chemodynamic effects and their promoted osteosarcoma destruction

As mentioned above, the LDH-Mn samples are black in color, indicating strong light absorption. Additionally, the thermal conductivity of the inner MgO layer is low, which is conducive to the increase in temperature. Both characteristics demonstrate excellent photothermal effects of the LDH-Mn samples. The temperature-elevation curves of the different samples under NIR laser irradiation (0.8 W/cm^2) are displayed in Fig. 4a and b. The temperature of the PEO sample slightly increased from 30 °C to 41 °C, while those of LDH-Mn1, LDH-Mn2, and LDH-Mn3 increased significantly from 30 °C to 52 °C, 55 °C, and 57 °C, respectively. The peroxidase-like activity of the LDH-Mn samples was detected using the TMB chromogenic assay. When TMB is oxidized by reactive oxygen species (ROS), an adsorption peak appears at 652 nm in the optical absorption spectrum [51]. As reported previously, Mn^{2+} and Mn^{3+} can produce ROS in the tumor microenvironment and therefore, are widely used in tumor therapy in the nanomedicine field [51,52]. The cumulative amount of Mn ions released from the various sample is in the order of: LDH-Mn3 > LDH-Mn2 > LDH-Mn1 (Fig. S3). In the presence of 100 μM H_2O_2, LDH-Mn2 and LDH-Mn3 produced some ROS, as revealed by the clearly increased absorption intensity of oxidized TMB at 652 nm, especially for the LDH-Mn3 sample (Fig. 4c).

Although LDHs have been widely developed as nanoreagents for cancer therapy, surface functionalization of Mg alloys via LDH for biomedical applications has only begun to be studied recently and is still in its infancy [13,53]. In our previous study, Mg–Al LDH and Mg–Fe LDH films were developed on Mg alloys, and both showed enhanced corrosion resistance and osteogenic effect [50,54]. However, Al is not safe for use in biodegradable implants, being related to neurotoxicity and dementia [55]. Mg–Fe LDH film showed a relatively weak photothermal conversion. Based on current results, Mn-contained LDH film on Mg alloy was confirmed as an advanced LDH-based film for the destruction

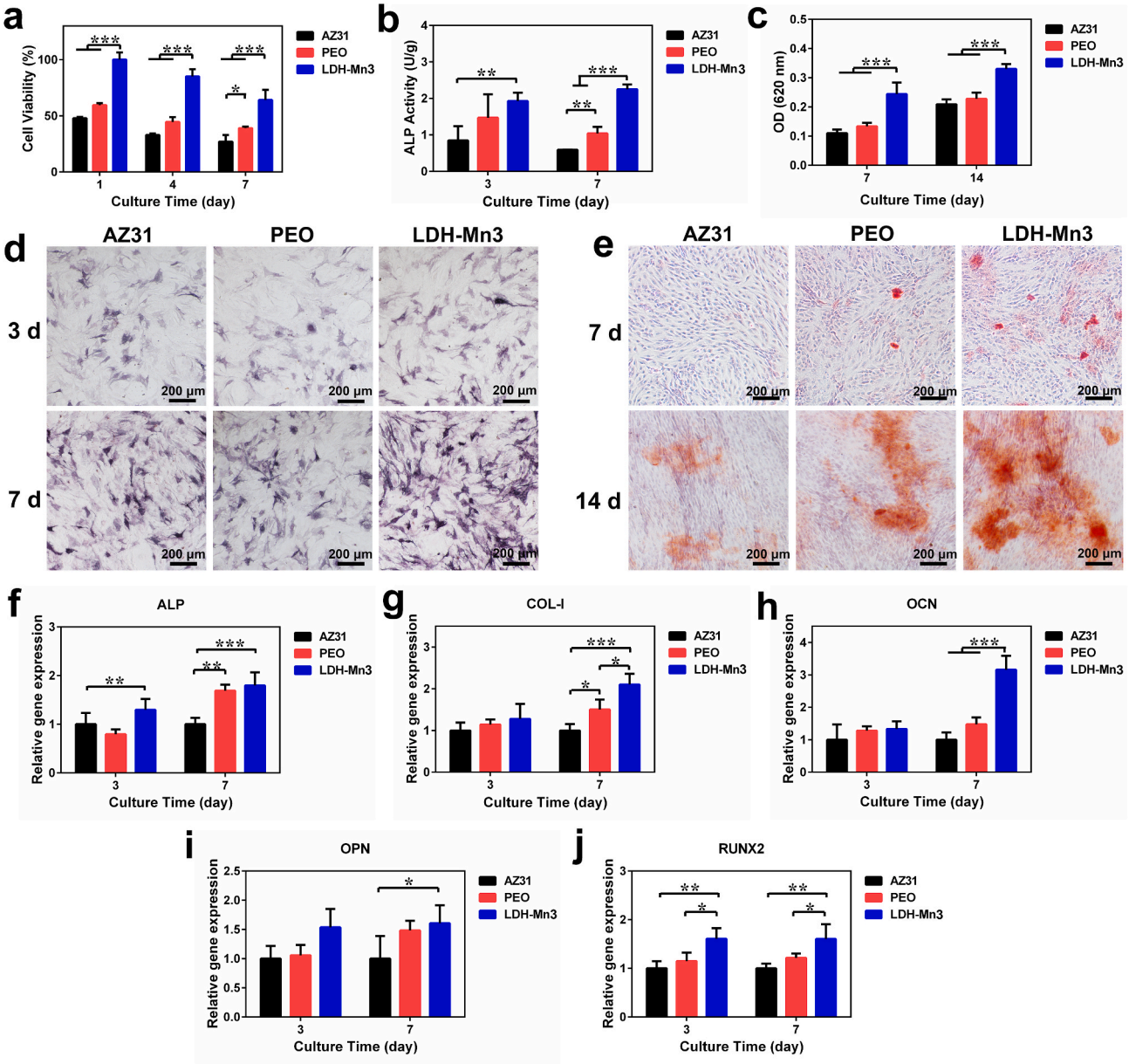

Fig. 6. *In vitro* evaluation of osteogenesis: (a) cell viability of C3H10T1/2 cells cultured in extracts of the various samples for 1, 4, and 7 days; (b–e) quantitative and qualitative results of matrix mineralization and ALP activity of C3H10T1/2 cells cultured in the extracts; and (f–j) expression of osteogenesis-related genes of C3H10T1/2 cells cultured in the extracts.

of osteosarcoma.

For *in vitro* tumor-killing evaluation, tumor cells (Sao-2) were seeded on the samples for four days, and then, the adhered cells were treated with or without NIR irradiation. In the absence of NIR irradiation, the number of cells on the LDH-Mn2 surface was larger than that on the PEO surface due to its improved biocompatibility (Fig. 4d). Fortunately, the number of Sao-2 cells on LDH-Mn3 clearly decreased because of its peroxidase activity. Furthermore, under NIR laser irradiation, the tumor cells on LDH-Mn3 were completely killed. To clearly visualize the live/dead cell distributions, the cells were further stained with calcein-AM and PI, and the result is shown in Fig. 4e. Evidently, the cells in the LDH-Mn3+NIR group dyed in red indicated that the tumor cells were almost killed.

The *in vivo* tumor destruction ability of LDH-Mn3 was investigated considering its excellent antitumor performance *in vitro*. Tumor cells were subcutaneously injected into the back of the Balb/c nude mice. When the tumor volume reached 250 mm^3, AZ31 and LDH-Mn3 samples were implanted *in situ*, followed by local NIR laser irradiation. The *in vivo* photothermal conversion of LDH-Mn3 was measured and a temperature increase of 14 °C was recorded (Fig. 4f). From the images displayed in Fig. 4g, the tumor volumes of the various groups were in the following descending order: AZ31 > LDH-Mn3 > LDH-Mn3 + NIR. The xenografts of mice in the LDH-Mn3 group were a little smaller than those in the AZ31 group, exhibiting a minor therapeutic performance. With further NIR irradiation, the tumor growth was significantly suppressed. The time-dependent tumor-growth curves confirmed the results. Additionally, the stability of the mice's body weights indicated that the health status of mice in each group was maintained (Fig. 4i). The pathological analyses, including H&E, TUNEL, and Ki67 of tumor tissues after different treatments were further conducted to clearly visualize the tumor-cell distributions (Fig. 4j). Tumor tissue from the LDH-Mn3 + NIR group showed fewer tumor-cell nuclei in the H&E images than the other groups. From the TUNEL and Ki67-stained microscopic images, significant apoptosis and restricted proliferation were also observed in the

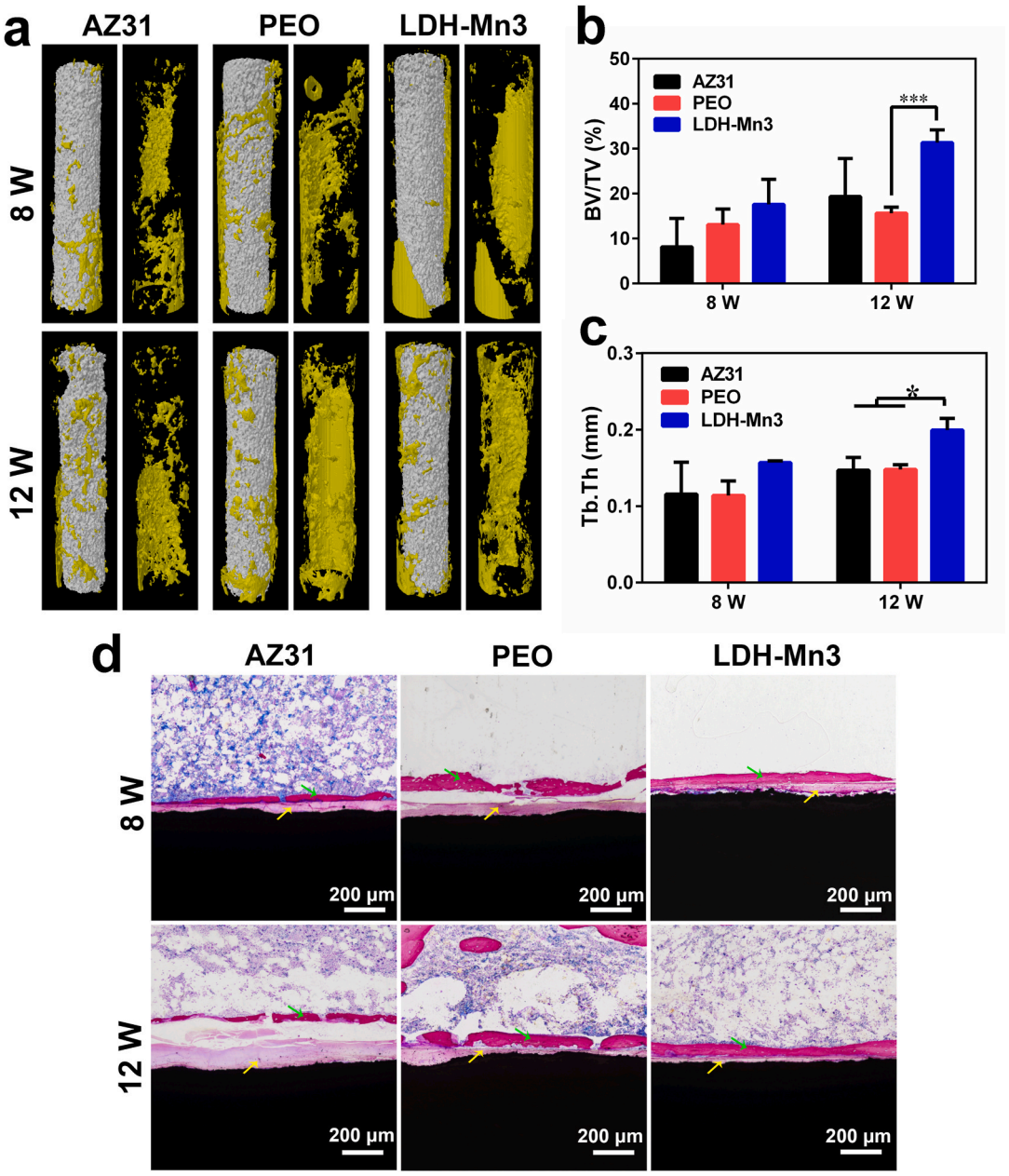

Fig. 7. Three-dimensional reconstruction images of Micro-CT results of the various samples after implantation in femur of SD rat for 8 and 12 weeks (a), yellow section indicate new bone. Calculated bone volume/tissue volume (BV/TV) (b) and trabecular thickness (Tb.Th) of the various samples after implantation for 8 and 12 weeks (c). VG staining of the various samples after femur implantation for 8 and 12 weeks (d).

LDH-Mn3 + NIR group. Overall, all results revealed that the LDH-Mn3 sample showed an effective tumor-killing ability due to its photothermal and chemodynamic effects.

3.5. Photothermal anti-bacterial activity

Implant-related infections often cause failures, introducing a series of clinical problems such as insufficient osteointegration and second surgery. Incorporating antibacterial agents, such as antibiotics, Ag, Zn ions, and Cu ions, on the implant surface has been common in recent years [56]. However, the potential toxicity and side effects of the antibacterial agents limit their further application [57]. Recently, implants with photothermal antibacterial properties have received great attention due to their controllability and rapid sterilization [58]. To study the photothermal antibacterial activity of the black LDH-coated Mg alloy specimens, the typical gram-negative bacteria (*S. aureus*) and gram-positive bacteria (*E. coli*) were incubated on the various samples for 12 h and then treated with or without NIR light irradiation. Since the PEO coating is porous and mainly composed of alkaline MgO, it shows poor biocompatibility, resulting in a few bacterial colonies on the PEO sample (Fig. 5). In contrast, the antibacterial ability of the LDH group was reduced because LDH-Mn samples showed excellent biocompatibility. Fortunately, under NIR irradiation, seriously damaged bacterial membranes and a reduction in both *S. aureus* and *E. coli* colonies were observed on the LDH-Mn3 samples. Heat-induced cell membrane damage causes cytoplasm leakage, thereby resulting in bacterial death. Overall, these results indicate that the constructed Mn-contained LDH films exhibit good photothermal antibacterial performance and have a high potential for preventing implant infection.

3.6. In vitro and in vivo osteogenesis

Effective osteogenesis is a critical step in the treatment of osteosarcoma and bone defect repair. Numerous studies have indicated that both Mg and Mn ions show excellent osteopromotive properties [59]. Zhang et al. proved that Mg ions can accelerate bone formation by promoting the release of calcitonin gene-related peptides (CGRP) [60]. The osteogenic effect of Mn ions, such as regulating parathyroid hormone (PTH) signaling pathway (a key calcium regulator) has also been widely reported [61,62]. In addition, good corrosion resistance and biocompatibility can improve the extracellular environment and support their survival, based on which the osteogenic capability of the extracts from the constructed LDH-coated Mg alloy was investigated. First, the cytotoxicity of these extracts was measured. Compared with raw AZ31 alloy and PEO groups, the LDH-Mn3 group showed better cell viability (Fig. 6a), and the result is consistent with the data in Fig. 3. Alkaline phosphatase activity (ALP) and extracellular matrix mineralization (ECM) were evaluated to assess the *in vitro* osteogenic induction abilities of the LDH-Mn3 sample. As displayed in Fig. 6b–e, both qualitative and quantitative results indicate that the LDH-Mn3 group showed the highest ECM mineralization and ALP activity. Besides, the expression of the osteogenic genes (ALP, COL-1, OCN, OPN, and RUNX2) further confirmed the excellent osteoinduction performance of the LDH-Mn3 group compared with AZ31 and PEO groups both on days 3 and 7 (Fig. 6f–j). The LDH-Mn3 sample facilitates *in vitro* cell differentiation when considered together, suggesting *in vivo* osteogenic activities is possible.

Thus, *in vivo* osteogenic bioactivity of LDH-Mn3 was further evaluated by implanting the sample into the femur of SD rats for 8 and 12 weeks. According to the 3D-reconstruction of the micro-CT images displayed in Fig. 7a, obvious local corrosion was observed on the AZ31 sample, while the PEO and LDH-Mn3 samples relatively maintained the original shape after 12 weeks of implantation. This result indicates that PEO and LDH-Mn3 samples showed better corrosion resistance in the bone tissue. Additionally, more new bone (in yellow) was observed on the LDH-Mn3 sample than on the other groups at week 8, and this trend was maintained till week 12. Besides, the fundamental parameters, including the BV/TV and Tb.Th were quantitatively analyzed, and the results are shown in Fig. 7b and c, respectively. After implantation for 12 weeks, the LDH-Mn3 sample exhibited higher BV/TV and Tb.Th values, as expected, thereby indicating the best osteogenic induction ability. Furthermore, micro-observation of the new bone tissue around implants was conducted by VG staining, and the result is shown in Fig. 7d. AZ31 implant experienced the most significant corrosion, as revealed by the thick corrosion layer (yellow arrow) formed after 12-week implantation. In contrast, apart from the thin corrosion layer, a significant new bone layer (green arrow) was observed surrounding the LDH-Mn3 implant. Considered together, all these observations confirmed the superior osteogenic induction ability of the LDH-Mn3 implants.

4. Conclusion

Biofunctional Mn-containing LDH nanosheet-engineered biodegradable Mg-based metallic implants were successfully constructed for OS therapeutics. The black LDH films could effectively control corrosion and release of Mg and Mn ions of Mg implants, thus significantly improve the cells adhesion, spreading, proliferation, and osteogenic differentiation *in vitro* and accelerate osteogenesis *in vivo*. Furthermore, the bone tumor cells/tissues were effectively killed by the black LDH film *in vitro* and *in vivo* due to its excellent photothermal effect and nanocatalytic Fenton-like performance. Also, the prepared LDH film exhibited superior photothermal antibacterial ability. Our results revealed that the constructed black Mn-containing LDH-modified biodegradable Mg metals might be a promising orthopedic implant for bone tumor therapy and related tissue defect regeneration.

CRediT authorship contribution statement

Dongdong Zhang: Conceptualization, Experiments, Data curation, Writing – original draft, Writing – review & editing. **Shi Cheng:** Conceptualization, Experiments, Data curation, Writing – original draft, Writing – review & editing. **Ji Tan:** Writing – review & editing. **Juning Xie:** Animal experiment, Writing – review & editing. **Yu Zhang:** Conceptualization, Supervision, Writing – review & editing. **Shuhan Chen:** Writing – review & editing. **Huihui Du:** Writing – review & editing. **Shi Qian:** Writing – review & editing. **Yuqing Qiao:** Writing – review & editing. **Feng Peng:** Supervision, Writing – review & editing. **Xuanyong Liu:** Conceptualization, Supervision, Writing – review & editing.

Declaration of competing interest

The authors declare no conflict of interest.

Acknowledgments

This work is financially supported by the National Key R&D Program of China (2021YFC2400500), National Natural Science Foundation of China (31771044), Shanghai Committee of Science and Technology, China (19JC1415500 and 20S31901200), High-end Entrepreneurial and Innovative Teams of Ningbo High-level Talents Project (2018A-09-C), S&T Innovation 2025 Major Special Programme of Ningbo (2020Z095) and S&T Industrial Programme of Cixi (2019gy01).

Appendix A. Supplementary data

Supplementary data to this article can be found online at https://doi.org/10.1016/j.bioactmat.2022.01.032.

References

[1] J. Ritter, S.S. Bielack, Osteosarcoma, Ann. Oncol. 21 (7) (2010) 320–325.
[2] M. Kansara, M.W. Teng, M.J. Smyth, D.M. Thomas, Translation biology of osteosarcoma, Nat. Rev. Cancer 14 (11) (2014) 722–735.
[3] R.J. Grimer, Surgical options for children with osteosarcoma, Lancet Oncol. 6 (2) (2005) 85–92.
[4] K. Zils, S. Bielack, M. Wilhelm, M. Werner, R. Schwarz, R. Windhager, G. Hofmann-Wackersreuther, T. Andus, L. Kager, T. Kuehne, P. Reichardt, T. Von Kalle, Osteosarcoma of the mobile spine, Ann. Oncol. 24 (8) (2014) 2190–2195.
[5] A.H.P. Loh, H.Y. Wu, A. Bahrami, F. Navid, M.B. McCarville, C. Wang, J.R. Wu, M. W. Bishop, N.C. Daw, M.D. Neel, B.N. Rao, Influence of bony resection margins and surgicopathological factors on outcomes in limb-sparing surgery for extremity osteosarcoma, Pediatr. Blood Cancer 62 (2) (2015) 246–251.
[6] W.J. Zhang, I. Bado, H. Wang, H.C. Lo, X. Zhang, Bone Metastasis: find your niche and fit in, Trends Cancer 5 (2) (2019) 95–110.
[7] H.S. Ma, C. Jiang, D. Zhai, Y.X. Luo, Y. Chen, F. Lv, Z.F. Yi, Y. Deng, J.W. Wang, J. Chang, C.T. Wu, A bifunctional biomaterial with photothermal effect for tumor therapy and bone regeneration Adv. Funct, Materials 26 (2016) 1197–1208.
[8] Y.Q. Liu, T. Li, H.S. Ma, D. Zhai, C.J. Deng, J.W. Wang, S.G. Zhuo, J. Chang, C. T. Wu, 3D-printed scaffolds with bioactive elements-induced photothermal effect for bone tumor therapy, Acta Biomater. 73 (2018) 531–546.
[9] L.Y. Wang, Q.H. Yang, M.F. Huo, D. Lu, Y.S. Gao, Y. Chen, H.X. Xu, Engineering single-atomic iron-catalyst-integrated 3D-printed bioscaffolds for osteosarcoma destruction with antibacterial and bone defect regeneration bioactivity, Adv. Mater. 33 (2021) 2100150.
[10] H.S. Ma, J. Luo, Z. Sun, L.G. Xia, M.C. Shi, M.Y. Liu, J. Chang, C.T. Wu, 3D printing of biomaterials with mussel-inspired nanostructures for tumor therapy and tissue regeneration, Biomaterials 111 (2016) 138–148.
[11] X. Li, X.M. Liu, S.L. Wu, K.W.K. Yeung, Y.F. Zheng, P.K. Chu, Design of magnesium alloys with controllable degradation for biomedical implants: from bulk to surface, Acta Biomater. 45 (2016) 2–30.
[12] M. Ali, A.E. Elsherif, A.U. Salih, M.A. Hamid, S. Hussein, A.K. Park, H. Yetisen, Butt, Surface modification and cytotoxicity of Mg-based bio-alloys: an overview of recent advances, J. Alloys Compd. 825 (2020) 154140.
[13] D.D. Zhang, F. Peng, X.Y. Liu, Protection of magnesium alloys: from physical barrier coating to smart self-healing coating, J. Alloys Compd. 853 (2020) 157010.
[14] H.F. Li, Y.F. Zheng, L. Qin, Progress of biodegradable metals, Prog. Nat. Sci. 24 (5) (2014) 414–422.
[15] L.D. Hou, Z. Li, Y. Pan, M. Sabir, Y.F. Zheng, L. Li, A review on biodegradable materials for cardiovascular stent application, Front, Mater. Sci. 10 (2016) 238–259.

[16] Y. Liu, Y.F. Zheng, X.H. Chen, J.A. Yang, H.B. Pan, D.F. Chen, L.N. Wang, J. L. Zhang, D.H. Zhu, S.L. Wu, K.W.K. Yeung, R.C. Zeng, Y. Han, S.k. Guan, Fundamental theory of biodegradazble metals-definition, criteria, and design, Adv. Funt. Mater 29 (2019) 201805452.

[17] V.V. Ramalingam, P. Ramasamy, M.D. Kovukkal, G. Myilsamy, Research and development in magnesium alloys for industrial and biomedical application: a Review, Met. Mater, Bar Int. 26 (2020) 409–430.

[18] L.D. Liu, F. Peng, D.D. Zhang, M. Li, J. Huang, X.Y. Liu, A tightly bonded reduced graphene oxide coating on magnesium alloy with photothermal effect for tumor therapy, J. Magnes. Alloys (2021), https://doi.org/10.1016/j.jma.2021.03.003.

[19] M. Li, M.Y. Yao, W.D. Wang, P. Wan, X. Chu, Y.F. Zheng, K. Yang, Y. Zhang, Nitrogen-containing bisphosphonate-loaded micro-arc oxidation coating for biodegradable magnesium alloy pellets inhibits osteosarcoma through targeting of the mevalonate pathway, Acta Biomater. 121 (2021) 682–694.

[20] H. Yao, L. Wu, G.S. Huang, B. Jiang, A. Atrens, F.S. Pan, Superhydrophobic coating for corrosion protection of magnesium alloys, J. Mater. Sci. Technol. 52 (2020) 100–118.

[21] M.J. Anjum, J.M. Zhao, H. Adi, M. Tabish, H. Murtaza, G.L. Yasin, M.U. Malik, W. Q. Khan, A review on self-healing coatings applied to Mg alloys and their electrochemical evaluation techniques, Int. J. Electrochem. Sci. 15 (2020) 3040–3053.

[22] J.E. Gray, B. Luan, Protective coatings on magnesium and its alloys-a critical review, J. Alloys Compd. 336 (2002) 88–113.

[23] M. Esmaily, J.E. Svensson, S. Fajardo, N. Birbilis, G.S. Frankel, S. Virtanen, R. Arrabal, S. Thomas, L.G. Johansson, Fundamentals and advances in magnesium alloy corrosion, Prog. Mater. Sci. 89 (2017) 92, 193.

[24] G.B. Dardand, M. Aliofkhazraei, P. Hamghalam, N. Valizade, Plasma electrolytic oxidation of magnesium and its alloys: mechanism, properties and applications, J. Magnes. Alloys 5 (2017) 74–132.

[25] H.C. Qian, D. Xu, C.W. Du, D.W. Zhang, X.G. Li, L.Y. Huang, et al., Dual-action smart coatings with a self-healing superhydrophobic surface and anti-corrosion properties, J. Mater. Chem. A 5 (2017) 2355–2364.

[26] A. Fattah-alhosseini, M. Molaei, M. Nouri, K. Babaei, Antibacterial activity of bioceramic coatings on Mg and its alloys created by plasma electrolytic oxidation (PEO): a review, J. Magnes. Alloys (2021), https://doi.org/10.1016/j.jma.2021.05.020.

[27] D.H. Wang, J. Tan, H.Q. Zhu, Y.F. Mei, X.Y. Liu, Biomedical implants with charge-transfer monitoring and regulation abilities, Adv. Sci. 8 (2021) 2004393.

[28] F. Peng, D. Wang, D. Zhang, B. Yan, H. Cao, Y. Qiao, X. Liu, PEO/Mg-Zn-Al LDH composite coating on Mg alloy as a Zn/Mg ion-release platform with multifunctions: enhanced corrosion resistance, osteogenic, and antibacterial activities, ACS Biomater. Sci. Eng. 4 (2018) 4112–4121.

[29] L. Cheng, C. Wang, L. Feng, L. Yang, Z. Liu, Functional nanomaterials for phototherapies of cancer, Chem. Rev. 114 (2014) 10869–10939.

[30] W.C. Wu, Y.Y. Pu, X.Y. Lu, H. Lin, J.L. Shi, Transitional Metal-based Noncatalytic medicine for tumor therapy, Adv. Healthc. Mater 10 (11) (2021) 2001819.

[31] J.J. Chen, Y.F. Zhu, C.T. Wu, J.L. Shi, Nanoplatform-based cascade engineering for cancer therapy, Chem. Soc. Rev. 49 (2020) 9057–9094.

[32] B.W. Yang, Y. Chen, J.L. Shi, Nanocatalytic medicine, Adv. Mater. 31 (39) (2019) 1901778.

[33] J. Yu, Q. Wang, D. O'Hare, L. Sun, Preparation of two dimensional layered double hydroxide nanosheets and their applications, Chem. Soc. Rev. 46 (2017) 5950–5974.

[34] Q. Wang, D. O'Hare, Recent advances in the synthesis and application of layered double hydroxide (LDH) nanosheets, Chem. Rev. 112 (2012) 4124–4155.

[35] M.Q. Zhao, Q. Zhang, J.Q. Huang, F. Wei, Hierarchical Nanocomposites derived from nanocarbons and layered double hydroxides - properties, synthesis, and applications, Adv. Funct. Mater. 22 (2012) 675–694.

[36] Z.Y. Cai, X.M. Bu, P. Wang, J.C. Ho, J.H. Yang, X.Y. Wang, Recent advances in layered double hydroxide electrocatalysts for the oxygen evolution reaction, J. Mater. Chem. A 7 (2019) 5069–5089.

[37] L. Mohapatra, K. Parida, A review on the recent progress, challenges and perspective of layered double hydroxides as promising photocatalysts, J. Mater. Chem. A 4 (2016) 10744.

[38] B. Li, Z. Gu, N. Kurniawan, W.Y. Chen, Z.P. Xu, Manganese-based layered double hydroxide nanoparticles as a T_1-MRI contrast agent with ultrasensitive pH response and high relaxivity, Adv. Mater. 29 (2017) 1700373.

[39] R.G. Lima Goncalves, H.M. Mendes, S.L. Bastos, L.C. D'Agostino, J. Tronto, S. H. Pulcinelli, C.V. Santilli, J. Leal Neto, Fenton-like degradation of methylene blue using Mg/Fe and MnMg/Fe layered double hydroxides as reusable catalysts, Appl. Clay Sci. 187 (2020) 105477.

[40] T. Jia, Z. Wang, Q.Q. Sun, S.M. Dong, J.T. Xu, F.M. Zhang, L.L. Peng, F. He, D. Yang, P.P. Yang, J. Lin, Intelligent Fe-Mn layered double hydroxides nanosheets anchored with upconversion nanoparticles for oxygen-elevated synergetic therapy and bioimaging, Small 16 (46) (2020) 2001343.

[41] Z.Y. Du, H.J. Leng, L.Y. Guo, Y.Q. Huang, T.Y. Zheng, Z.D. Zhao, X. Liu, X. Zhang, Q. Cai, X.P. Yang, Calcium silicate scaffolds promoting bone regeneration via the doping of Mg^{2+} or Mn^{2+} ion, Compos. B Eng. 190 (2020) 107937.

[42] D.D. Zhang, F. Peng, J.J. Qiu, J. Tan, X.M. Zhang, S.H. Chen, S. Qian, X.Y. Liu, Regulating corrosion reactions to enhance the anti-corrosion and self-healing abilities of PEO coating on magnesium, Corrosion Sci. 192 (2021) 109840.

[43] N. Li, M.G. He, X.K. Lu, L. Liang, R. Li, B.B. Yan, G.Y. Chen, Enhanced norfloxacin degradation by visible–light–driven Mn_3O_4/γ–MnOOH photocatalysis under weak magnetic field, Sci. Total Environ. 761 (2021) 143268.

[44] F. Jia, Y. Meng, J.G. Wang, Y.L. Sun, Z.D. Wang, B. Zhao, X.T. Tao, G.J. Xu, Promoting diesel soot combustion efficiency by tailoring the shapes and crystal facets of nanoscale Mn_3O_4, Appl. Catal. B Environ. 242 (2019) 227–237.

[45] L. Hu, L. Zhang, Z.Q. Huang, W.J. Zhu, Z.J. Zhao, J.L. Gong, Facet–evolution growth of Mn_3O_4@$Co_xMn_{3-x}O_4$ electrocatalysts on Ni foam towards efficient oxygen evolution reaction, J. Catal. 369 (2019) 105–110.

[46] L. Guo, W. Wu, Y. Zhou, F. Zhang, R. Zeng, J. Zeng, Layered double hydroxide coatings on magnesium alloys: a review, J. Mater. Sci. Technol. 34 (2018) 1455–1466.

[47] F. Peng, D.H. Wang, Y.X. Tian, H.L. Cao, Y.Q. Qiao, X.Y. Liu, Sealing the pores of PEO coating with Mg-Al layered double hydroxide: enhanced corrosion resistance, cytocompatibility and drug delivery ability, Sci. Rep. 7 (2017).

[48] F. Peng, D. Wang, D. Zhang, B. Yan, H. Cao, Y. Qiao, X. Liu, PEO/Mg–Zn–Al LDH composite coating on Mg alloy as a Zn/Mg ion-release platform with multifunctions: enhanced corrosion resistance, osteogenic, and antibacterial activities, ACS Biomater. Sci. Eng. 4 (2018) 4112–4121.

[49] H. Li, F. Peng, D. Wang, Y. Qiao, D. Xu, X. Liu, Layered double hydroxide/poly-dopamine composite coating with surface heparinization on Mg alloys: improved anticorrosion, endothelialization and hemocompatibility, Biomater. Sci. 6 (2018) 1846–1858.

[50] F. Peng, H. Li, D. Wang, P. Tian, Y. Tian, G. Yuan, D. Xu, X. Liu, Enhanced corrosion resistance and biocompatibility of magnesium alloy by Mg-Al-layered double hydroxide, ACS Appl. Mater. Interfaces 8 (2016) 35033–35044.

[51] Y. Zhu, Y.J. Wang, G.R. Williams, L.Y. Fu, J.J. Wu, H. Wang, R.Z. Liang, X.S. Weng, M. Wei, Multicomponent transition metal dichalcogenide nanosheets for imaging-guided photothermal and chemodynamic therapy, Adv. Sci. 7 (2020) 2000272.

[52] L. Yan, Y.J. Wang, T.T. Hu, X. Mei, X.J. Zhao, Y.Y. Bian, L. Jin, R.Z. Liang, X. S. Weng, M. Wei, Layered double hydroxide nanosheets: towards ultrasensitive tumor microenvironment responsive synergistic therapy, J. Mater. Chem. B 8 (2020) 1445–1455.

[53] G. Choi, J.H. Choy, Recent progress in layered double hydroxides as a cancer theranostic nanoplatform, WIREs Nanomed, Nanobiotechnol 13 (2021), e1679.

[54] D.D. Zhang, J.L. Zhou, F. Peng, J. Tan, X.M. Zhang, S. Qian, Y.Q. Qiao, Y. Zhang, X. Y. Liu, Mg-Fe LDH sealed coating on magnesium for biodegradation control, antibacteria and osteogenesis, J. Mater. Sci. Technol. 105 (2022) 57–67.

[55] S. El-Rahman, Neuropathology of aluminum toxicity in rats (glutamate and GABA impairment), Pharmacol. Res. 47 (2003) 189–194.

[56] W.L. Li, E.S. Thian, M. Wang, Z.Y. Wang, L. Ren, Surface design for antibacterial materials: form fundamental to advanced strategies, Adv. Sci. (2021) 2100368.

[57] S.R. Snavely, G.R. Hodges, The neurotoxicity of antibacterial agents, Ann. Intern. Med. 101 (1984) 92–104.

[58] L. Tan, J. Li, X.M. Liu, Z.D. Cui, X.J. Yang, S.L. Zhu, Z.Y. Li, X.B. Yuan, Y.F. Zheng, K.W.K. Yeung, H.B. Pan, X.B. Wang, S.L. Wu, Rapid Biofilm Eradication on Bone Implants Using Red Phosphorus and Near-Infrared Light, vol. 20, 2018, p. 1801808.

[59] J.L. Wang, J.K. Xu, C. Hopkins, D.H.K. Chow, L. Qin, Biodegradable magnesium-based implants in orthopedics-A general review and perspectives, Adv. Sci. 7 (2020) 1902443.

[60] Y. Zhang, J. Xu, Y.C. Ruan, M.K. Yu, M. O'Laughlin, H. Wise, D. Chen, L. Tian, D. Shi, J. Wang, S. Chen, J.Q. Feng, D.H. Chow, X. Xie, L. Zheng, L. Huang, S. Huang, K. Leung, N. Lu, L. Zhao, H. Li, D. Zhao, X. Guo, K. Chan, F. Witte, H. C. Chan, Y. Zheng, L. Qin, Implant-derived magnesium induces local neuronal production of CGRP to improve bone-fracture healing in rats, Nat. Med. 22 (2016) 1160–1169.

[61] F. Lüthena, U. Bulnheima, P.D. Müller, J. Rychly, H. Jesswein, J.G.B. Nebe, Influence of manganese ions on cellular behavior of human osteoblasts in vitro, Biomol. Eng. 24 (2007) 531–536.

[62] E.M. Lewiwcki, P.D. Miller, Skeletal effects of primary hyperparathyroidism: bone mineral density and fracture risk, J. Clin. Densitom. 16 (2013) 28–32.